Mon. Not. R. Astron. Soc. **366,** 1253–1264 (2006) doi:10.1111/j.1365-2966.2005.09810.x

Gemini/GMOS spectra of globular clusters in the Leo group elliptical NGC 3379

Michael Pierce,[1⋆] Michael A. Beasley,[2] Duncan A. Forbes,[1] Terry Bridges,[3] Karl Gebhardt,[4] Favio Raul Faifer,[5,6] Juan Carlos Forte,[5] Stephen E. Zepf,[7] Ray Sharples,[8] David A. Hanes[3] and Robert Proctor[1]

[1]*Centre for Astrophysics and Supercomputing, Swinburne University, Hawthorn, VIC 3122, Australia*
[2]*Lick Observatory, University of California, Santa Cruz, CA 95064, USA*
[3]*Department of Physics, Queen's University, Kingston, Ontario, K7L 3N6, Canada*
[4]*Astronomy Department, University of Texas, Austin, TX 78712, USA*
[5]*Facultad de Cs. Astronomicas y Geofisicas, UNLP, Paseo del Bosque 1900, La Plata, and CONICET, Argentina*
[6]*IALP – CONICET, Argentina*
[7]*Department of Physics and Astronomy, Michigan State University, East Lansing, MI 48824, USA*
[8]*Department of Physics, University of Durham, South Road, Durham DH1 3LE*

Accepted 2005 November 1. Received 2005 October 31; in original form 2005 May 11

ABSTRACT

The Leo group elliptical NGC 3379 is one of the few normal elliptical galaxies close enough to make possible observations of resolved stellar populations, deep globular cluster (GC) photometry and high signal-to-noise ratio GC spectra. We have obtained Gemini/GMOS spectra for 22 GCs associated with NGC 3379. We derive ages, metallicities and α-element abundance ratios from simple stellar population models using the recent multi-index χ^2 minimization method of Proctor & Sansom. All of these GCs are found to be consistent with old ages, i.e. $\gtrsim$10 Gyr, with a wide range of metallicities. This is comparable to the ages and metallicities that Gregg et al. found a couple of years ago for resolved stellar populations in the outer regions of this elliptical. A trend of decreasing α-element abundance ratio with increasing metallicity is indicated.

The projected velocity dispersion of the GC system is consistent with being constant with radius. Non-parametric, isotropic models require a significant increase in the mass-to-light ratio at large radii. This result is in contrast to that of Romanowsky et al., who recently found a decrease in the velocity dispersion profile as determined from planetary nebulae (PN). Our constant dispersion requires a normal-sized dark halo, although without anisotropic models we cannot rigorously determine the dark halo mass.

A two-sided χ^2 test over all radii gives a 2σ difference between the mass profile derived from our GCs compared to the PN-derived mass model of Romanowsky et al. However, if we restrict our analysis to radii beyond one effective radius and test if the GC velocity dispersion is consistently higher, we determine a $> 3\sigma$ difference between the mass models, and hence we favour the conclusion that NGC 3379 does indeed have dark matter at large radii in its halo.

Key words: globular clusters: general – galaxies: individual: NGC 3379 – galaxies: kinematics and dynamics – galaxies: star clusters.

1 INTRODUCTION

The globular cluster (GC) systems of numerous elliptical galaxies have been well studied photometrically (e.g. Gebhardt & Kissler-Patig 1999; Kundu & Whitemore 2001; Larsen et al. 2001). Since the discovery of the bimodal colour distribution of GCs in elliptical galaxies (see Harris 1999 for a review), several models have been proposed to explain how these GC systems are formed.

Ashman & Zepf (1992) proposed that some, or all, of the high-metallicity GCs will be formed during gas-rich merger events and therefore be of a similar age to those mergers. For the case of a series of minor gaseous mergers, a roughly monotonic increase in metallicity is expected with decreasing age.

⋆E-mail: mpierce@astro.swin.edu.au

The multiphase collapse model of Forbes, Brodie & Grillmair (1997) proposed that the majority of GCs are native to their galaxy and formed during two, or more, protogalactic collapse phases. Red, metal-rich GCs are expected to be 2–4 Gyr younger than their blue, metal-poor counterparts according to the semi-analytic GC formation model of Beasley et al. (2002).

Cote, Marzke & West (1998) invoked tidal capture of GCs from dwarf galaxies to account for the blue GC population of large elliptical galaxies. A higher fraction of blue, metal-poor GCs is expected compared with spirals of a similar luminosity. Assuming that blue GCs form at the same time as their parent galaxy, 'down-sizing' (Cowie et al. 1996; Kodama et al. 2005) suggests that blue GCs captured from dwarf galaxies should be younger than the native blue GCs.

Thus a key discriminant of the formation models is GC age. Unfortunately, from photometry alone it is very difficult to determine the age and metallicity of individual GCs, owing to the age–metallicity degeneracy (Brodie et al. 2005), and therefore high-quality spectra are required. The stellar population properties of individual GCs can be measured accurately with low-resolution integrated spectra of sufficient signal-to-noise ratio (S/N $\geqslant$ 30). The age–metallicity degeneracy can be broken by measuring spectral Lick indices (Worthey 1994), and comparing those indices to single stellar population (SSP) models. High-S/N spectroscopic studies (i.e. those capable of determining ages for individual GCs) of elliptical galaxy GC systems are limited to around a dozen galaxies (e.g. NGC 1399, Forbes et al. 2001; NGC 1023, Larsen & Brodie 2002; NGC 1316, Goudfrooij et al. 2001; NGC 3610, Strader et al. 2003, Strader, Brodie & Forbes 2004; NGC 2434, 3379, 3585, 5846 and 7192, Puzia et al. 2004; NGC 5128, Peng, Ford & Freeman 2004; NGC 4365, Brodie et al. 2005; NGC 1052, Pierce et al. 2005). Except for Goudfrooij et al. and Peng et al., these works found the majority of GCs to be old (>10 Gyr) with a small fraction of young GCs for some galaxies.

In this work we report on the analysis of Gemini/GMOS spectra of a sample of GCs in NGC 3379. This is a typical, nearby (10.8 $\pm$ 0.6 Mpc, Gregg et al. 2004) E0/1 elliptical galaxy. It is of intermediate luminosity ($M_V = -21.06$), with typical early-type colours, Mg_2 index and velocity dispersion (Davies et al. 1987) for its luminosity. There is no sign of any optical disturbance (Schweizer & Seitzer 1992). There is, however, a small nuclear dust ring at a radius of 1.5 arcsec (van Dokkum & Franx 1995) and some ionized gas that extends to a radius of 8 arcsec (Macchetto et al. 1996).

NGC 3379 is one of only a few elliptical galaxies to lie close enough that its stars can be resolved by the *Hubble Space Telescope* (*HST*). Resolved stellar population measurements using the *HST* NICMOS camera in the *J* and *H* bands have been made by Gregg et al. (2004). Measuring individual stellar magnitudes and colours to just below the red giant branch (RGB) tip, they found the outer region stellar population to be old, with ages >8 Gyr and a mean metallicity around solar. They noted similarities to the Galactic bulge. For the central region, Terlevich & Forbes (2002) used Lick indices to estimate an age of 9.3 Gyr, [Fe/H] = +0.16 and [Mg/Fe] = +0.24. This suggests that radial age and metallicity variations are relatively small.

The *UBRI* photometry of the GC system of this galaxy reveals the classic GC colour bimodality (Whitlock, Forbes & Beasley 2003). Whitlock et al. estimate a GC specific frequency of $S_N = 1.1 \pm 0.6$, which is low for an elliptical galaxy, although it is important to remember that NGC 3379 belongs to a relatively small group of galaxies (Leo) and, therefore, a low S_N is not unexpected (Bridges 1992). The *BVR* photometry of Rhode & Zepf (2004) indicates a similarly low S_N of 1.2 ± 0.3 and that approximately 70 per cent of NGC 3379 GCs are blue.

To derive GC ages and metallicities, we measure Lick indices from our GMOS spectra. We then apply the multi-index χ^2 minimization method of Proctor & Sansom (2002), which employs all the available Lick indices to break the age–metallicity degeneracy and simultaneously measure the α-element abundance ratios [see Proctor, Forbes & Beasley (2004) for an application to Galactic GCs and Pierce et al. (2005) for NGC 1052 GCs].

In addition to the measurement of line indices, integrated spectra of GCs allow the measurement of recession velocities, which confirm whether the GCs are indeed associated with the galaxy being studied. With a large enough sample of measured GC velocities, it is possible to probe the gravitational potential and therefore the dark matter halo of a galaxy (e.g. Zepf et al. 2000; Cote et al. 2001, 2003; Peng et al. 2004; Richtler et al. 2004).

Measurements of planetary nebulae (PN) kinematics in NGC 3379 (Romanowsky et al. 2003) revealed a decreasing velocity dispersion profile at large radii. This suggested that NGC 3379 has a significantly lower mass-to-light ratio ($M/L = 7.1 \pm 0.6$ at 5 R_e) than most large ellipticals, indicating a minimal dark matter (DM) halo. This result would appear to be in conflict with the standard cold dark matter (CDM) galaxy formation picture in which all galaxies lie within significant DM haloes. Here we use the measured velocities of our sample of GCs, as well as the GC data of Puzia et al. (2004), as an alternative data set to test this important claim.

In this paper we present our GMOS observations and data reduction of GC spectra in Section 2. An analysis of ages, metallicities and α-element abundance ratios derived from Lick indices is presented in Section 3. In Section 4 we focus on GC kinematics and the implications for the dark matter halo of NGC 3379. We discuss our results in Section 5 and present our conclusions in Section 6.

2 OBSERVATIONS AND DATA REDUCTION

The observations described below are part of Gemini programme GN-2003A-Q-22. GC candidates were selected from Gemini North Multi-Object Spectrograph (GMOS; Hook et al. 2002) imaging, obtained during 2003 January, for three fields around NGC 3379. The data reduction and GC candidate selection process are almost identical to those of Forbes et al. (2004) for NGC N4649. Briefly, SExtractor (Bertin & Arnouts 1996) was used to select GC candidates based upon their Gemini zero-point colours ($0.7 < g - i < 1.4$), magnitudes ($i < 24$) and structural properties (i.e. objects with stellarity index >0.35). Interstellar reddening towards NGC 3379 is $E(B - V) = 0.024$ mag and is not taken into consideration (Schlegel, Finkbeiner & Davis 1998). Spectroscopy of NGC 3379 globular clusters were obtained with GMOS on the Gemini North telescope in the months of 2003 February and April. GMOS masks for three fields were designed, but only the central field was observed within the time allocation. Seeing was typically $\sim$0.9 arcsec.

The GMOS charge-coupled devices (CCDs) consist of three abutted 2048 $\times$ 4608 EEV chips with a plate scale of 0.0727 arcsec pixel^{-1} (unbinned). For our setup, we binned four times in the dispersion direction, yielding 1.84 Å per binned pixel, giving a final resolution of full width at half-maximum FWHM $\sim$4 Å. The dispersion runs across the detectors in the GMOS instrument, resulting in two $\sim$20 Å gaps in the dispersion direction of the spectra. The B600_G5303 grating was used, with central

wavelengths for successive exposures set alternately to 5000 and 5025 Å (in order to obtain full wavelength information across the gaps in the GMOS detectors). The effective wavelength range of each slitlet is a function of its position on the mask, but typically covered 3800–6660 Å. A slit width of 1.0 arcsec was chosen to match the seeing, and the minimum slit length was 6 arcsec, a compromise between maximizing the number of slitlets and allowing for reliable sky subtraction. Exposures of 20 × 1800 s were taken, yielding a total of 10 h on-source integration time. Bias frames, dome flat fields and copper–argon (CuAr) arc exposures were taken as part of the Gemini baseline calibrations.

These data were reduced using the Gemini/GMOS packages in IRAF and a number of custom-made scripts. From the CuAr arcs, wavelength solutions with typical residuals of 0.1 Å were achieved. Objects and sky regions in the object spectra were manually identified in cross-sections of the two-dimensional images. The spectra were then extracted by tracing them in the dispersion direction. After some experimentation, optimal (variance) extraction was found to yield the best results since our data are oversampled on the detector. In some cases, objects were too faint to trace individually and we therefore co-added several 2D images, taken adjacent in time, to act as a reference for the extractions. We verified beforehand that flexure was minimal between the reference images. Finally, the extracted spectra were median combined and weighted by their fluxes with cosmic ray rejection.

In the absence of any velocity standard stars, the recession velocities were measured by using four Bruzual & Charlot (2003) model stellar energy distributions (SEDs) for old ages with metallicities [Fe/H] = −2.25, −1.64, −0.64 and −0.33. The task FXCOR in IRAF was used and the average (weighted by the cross-correlation peak height) was taken. Objects with recession velocities in the range $900 \pm 400\,\mathrm{km\,s^{-1}}$ are potentially associated with NGC 3379. These are presented in Table 1 and also used in our kinematic analysis in Section 4. There was one foreground star and one background galaxy out of the 24 spectra obtained. Our low contamination rate of 9 per cent is due to good imaging and colour selection. We note that the spectrum of g1420 shows emission lines, most notably 4959 and 5007 Å [O III], which we assume are due to a planetary nebula (see Fig. 1). Minniti & Rejkuba (2002) report a similar discovery for a GC in NGC 5128, and provide a discussion of the implications. Another GC, g1426, shows unexplained emission features around ∼5000 Å.

A first-order flux calibration was carried out by normalizing the spectra with a low-order polynomial. In order to measure Lick indices, we convolved our spectra with a wavelength-dependent Gaussian kernel to match the resolution of the Lick/IDS system (see Beasley et al. 2004b). Lick indices (Trager et al. 1998) were measured from our normalized spectra. Owing to the variable wavelength ranges in these spectra, the same set of indices could not be measured for all spectra. However, all covered a wavelength range of 4500–5500 Å. Uncertainties in the indices were derived from the photon noise in the unfluxed spectra. No Lick standard stars were observed, so we therefore cannot fully calibrate the GCs on to the Lick system. Consequently, there are some systematic differences between some of the measured indices and those used in the SSP models. These issues are discussed further in Sections 3 and 5. Measured line indices and uncertainties are presented in Tables 2 and 3.

The final spectra have S/N = 18–58 $\mathrm{Å^{-1}}$ at 5000 Å, giving errors in the Hβ index of 0.13–0.44 Å. (We note that g1566 has an Hβ error of ±0.065 Å and S/N = 118. However this is not representative, as this GC is ∼1.5 mag brighter than any other.)

Table 1. Confirmed globular clusters around NGC 3379. Cluster ID, coordinates, g magnitude, and $g-r$ and $g-i$ colours are from our GMOS imaging and are instrumental magnitudes only. Heliocentric velocities are from the spectra presented in this work.

ID	RA (J2000) (h m s)	Dec. (J2000) (° ′ ″)	g (mag)	$g-r$ (mag)	$g-i$ (mag)	$V_{\rm helio}$ (km s^{-1})
g1566	10:47:50.5	12:34:37.2	19.83	0.65	0.96	1071 ± 18
g296	10:48:02.2	12:35:57.6	21.40	0.62	0.88	1022 ± 52
g1940	10:47:48.2	12:35:45.3	21.42	0.74	0.90	875 ± 25
g1550	10:47:53.6	12:34:54:6	21.47	0.71	1.09	1100 ± 31
g2122	10:47:47.7	12:34:14.8	21.49	0.74	0.93	922 ± 32
g1078	10:47:54.2	12:36:31.9	21.54	0.70	1.00	1000 ± 24
g1420	10:47:50.7	12:35:32.3	21.54	0.62	0.90	764 ± 38
g1540	10:47:53.5	12:35:04.9	21.68	0.58	0.83	790 ± 41
g1617	10:47:50.4	12:33:47.8	21.88	0.62	0.96	650 ± 37
g1588	10:47:49.7	12:34:10.2	22.32	0.60	1.10	546 ± 45
g114	10:48:04.9	12:35:38.5	22.35	0.61	0.90	861 ± 45
g1426	10:47:50.6	12:35:19.2	22.37	0.61	0.87	797 ± 71
g1610	10:47:58.9	12:33:54.5	22.39	0.55	0.79	957 ± 61
g1571	10:47:49.7	12:34:32.8	22.47	0.72	1.04	744 ± 28
g1519	10:47:49.6	12:35:27.0	22.49	0.73	1.16	623 ± 42
g1934	10:47:47.9	12:36:23.4	22.72	0.64	0.76	1004 ± 65
g1580	10:47:54.2	12:34:21.6	22.84	0.71	1.09	1066 ± 32
g219	10:48:01.8	12:37:22.0	23.04	0.57	0.85	868 ± 95
g1893	10:47:45.1	12:37:53.0	23.26	0.86	1.21	804 ± 43
g1630	10:47:50.5	12:36:11.8	23.65	0.77	1.21	1115 ± 61
g1595	10:47:52.9	12:34:04.4	23.69	0.67	1.00	970 ± 70
g230	10:48:01.2	12:37:06.9	23.93	0.80	1.28	1022 ± 90

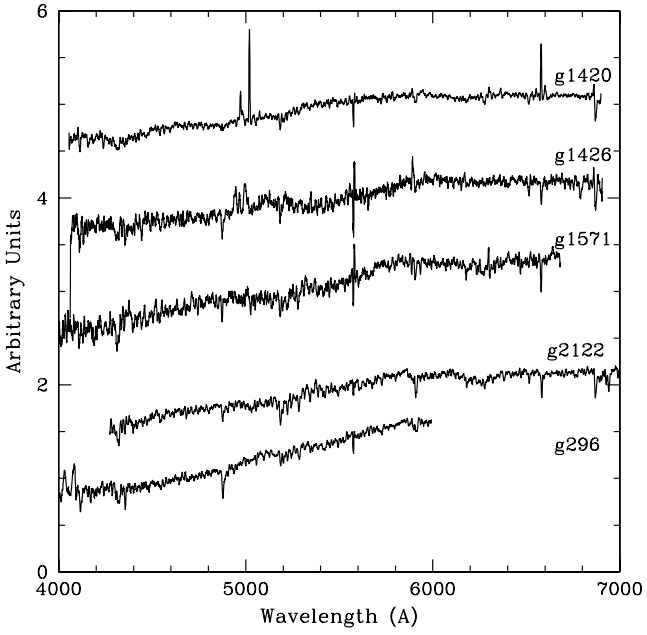

Figure 1. Normalized GC spectra, which have been offset by one unit, and have not been de-redshifted. These sample spectra show the wavelength range that the majority of our spectra cover and display the range of S/N and metallicity present. The spectrum of g1426 shows emission features around 5000 and 5890 Å of unknown origin. The PN hosting GC, g1420, is also plotted and the emission due to 4959 and 5007 Å [O III] lines can be seen redshifted to 4971 and 5019 Å.

Table 2. Globular cluster indices $\lambda < 4600$ Å: central index values (first line) and errors (second line). Indices in brackets are removed during the fitting process. Missing values are due to limited wavelength coverage.

ID	$H\delta_A$ (Å)	$H\delta_F$ (Å)	CN_1 (mag)	CN_2 (mag)	Ca4227 (Å)	*G* band (Å)	$H\gamma_A$ (Å)	$H\gamma_F$ (Å)	Fe4383 (Å)	Ca4455 (Å)	Fe4531 (Å)
g1566	...	...	...	...	0.493	3.106	−0.962	0.896	2.365	0.591	2.008
	...	...	...	...	0.069	0.117	0.119	0.073	0.167	0.084	0.124
g296	(4.054)	(3.555)	(0.002)	(0.038)	0.481	2.887	−0.409	1.019	0.707	0.794	0.856
	(0.253)	(0.166)	(0.008)	(0.009)	0.138	0.237	0.238	0.148	0.353	0.173	0.266
g1940	...	...	...	...	...	3.256	−0.919	0.437	1.207	0.514	2.532
	...	...	...	...	...	0.235	0.237	0.151	0.342	0.169	0.243
g1550	...	1.302	(0.057)	(0.106)	0.681	4.005	(−4.947)	(−1.474)	3.992	(0.467)	3.044
	...	0.205	(0.008)	(0.010)	0.151	0.246	(0.273)	(0.173)	0.342	(0.179)	0.255
g2122	...	...	...	...	...	5.555	−5.405	−1.191	4.199	(0.866)	3.108
	...	...	...	...	...	0.251	0.295	0.184	0.363	(0.185)	0.266
g1078	0.865	1.694	(0.010)	(0.043)	0.588	3.866	−1.420	0.486	(1.280)	(0.285)	2.309
	0.291	0.195	(0.008)	(0.009)	0.146	0.241	0.249	0.157	(0.354)	(0.177)	0.250
g1420	...	(1.278)	(0.019)	(0.049)	(1.089)	2.719	−0.457	(0.541)	0.763	0.504	(0.770)
	...	(0.193)	(0.008)	(0.009)	(0.139)	0.254	0.249	(0.159)	0.366	0.178	(0.266)
g1540	3.926	2.973	(−0.057)	(−0.053)	0.439	2.091	0.367	(1.201)	0.877	0.477	0.846
	0.270	0.185	(0.008)	(0.009)	0.149	0.255	0.245	(0.155)	0.369	0.182	0.277
g1617	...	(0.724)	(−0.021)	(0.017)	(0.191)	3.743	−1.765	0.525	2.259	0.447	1.943
	...	(0.240)	(0.009)	(0.011)	(0.177)	0.292	0.302	0.188	0.415	0.209	0.305
g1588	...	...	...	...	1.192	4.292	(−4.894)	−0.283	3.098	0.837	3.327
	...	...	...	...	0.213	0.350	(0.386)	0.234	0.492	0.249	0.356
g114	(0.829)	2.917	(−0.079)	(−0.079)	(−0.314)	2.070	0.402	1.935	0.551	0.648	(−0.256)
	(0.432)	0.270	(0.012)	(0.014)	(0.221)	0.382	0.357	0.218	0.534	0.259	(0.398)
g1426	...	2.368	(−0.037)	(−0.008)	(−0.208)	4.122	0.267	0.525	0.860	0.051	1.447
	...	0.268	(0.011)	(0.013)	(0.218)	0.342	0.351	0.230	0.521	0.259	0.389
g1610	(4.667)	3.479	(−0.234)	(−0.232)	0.175	(−2.291)	−1.207	0.580	1.182	0.678	1.332
	(0.380)	0.261	(0.012)	(0.014)	0.215	(0.433)	0.363	0.229	0.520	0.250	0.390
g1571	(3.298)	(1.842)	(0.001)	(0.042)	0.859	(6.656)	(−8.418)	−1.715	6.113	2.101	2.561
	(0.439)	(0.315)	(0.013)	(0.015)	0.230	(0.350)	(0.448)	0.268	0.498	0.260	0.397
g1519	...	...	...	...	1.238	3.570	−2.920	0.183	3.012	0.952	2.863
	...	...	...	...	0.205	0.369	0.389	0.239	0.515	0.252	0.366
g1934	...	...	...	...	...	0.262	1.058	1.875	−0.069	0.517	−0.171
	...	...	...	...	...	0.427	0.384	0.238	0.606	0.300	0.462
g1580	−1.848	(−1.852)	(0.177)	(0.129)	(−1.926)	3.971	−5.028	−0.634	5.124	2.185	(0.530)
	0.659	(0.475)	(0.017)	(0.020)	(0.367)	0.487	0.526	0.323	0.631	0.308	(0.494)
g219	(−4.486)	(0.019)	(0.037)	(0.188)	(2.267)	−1.395	4.035	(1.342)	0.040	−0.334	−0.274
	(0.665)	(0.422)	(0.016)	(0.018)	(0.253)	0.613	0.473	(0.325)	0.767	0.385	0.559
g1893	...	...	...	...	...	...	...	...	...	...	2.245
	...	...	...	...	...	...	...	...	...	...	0.602
g1630	...	(−5.925)	(0.150)	(0.121)	(3.212)	5.462	−8.396	−1.286	6.183	(−1.965)	(5.771)
	...	(0.927)	(0.025)	(0.029)	(0.339)	0.650	0.851	0.487	0.960	(0.555)	(0.615)
g1595	(−0.313)	(−3.507)	(−0.182)	(−0.060)	−0.684	−2.792	2.502	(4.899)	(7.957)	(3.874)	(5.532)
	(1.160)	(0.986)	(0.030)	(0.034)	0.575	1.038	0.761	(0.414)	(0.961)	(0.498)	(0.773)
g230	(11.407)	2.689	(−0.644)	(−0.585)	(−3.332)	(−4.732)	2.696	(−3.572)	(−3.244)	−0.978	(6.999)
	(0.813)	0.766	(0.028)	(0.031)	(0.645)	(1.047)	0.726	(0.612)	(1.213)	0.556	(0.671)

3 AGES, METALLICITIES AND α-ELEMENT ABUNDANCE RATIOS

In this section we describe how we derive ages, metallicities and α-element abundances. The resulting values are listed in Table 4.

We apply the χ^2 multi-index fitting technique of Proctor & Sansom (2002) for this analysis. This method involves the comparison of the measured Lick indices with SSP models [its application to extragalactic GCs is described fully in Pierce et al. (2005)]. The SSP models of Thomas, Maraston & Korn (2004, hereafter TMK04) were chosen because they present the only set of models that include the effect of α-element abundance ratios on the Balmer lines.

We compare the measured Lick indices to the TMK04 SSPs and obtain a minimum χ^2 fit. This fit is obtained using all the indices

Table 3. Globular cluster indices $\lambda > 4600$ Å: central index values (first line) and errors (second line). Indices in brackets are removed during the fitting process. Missing values are due to limited wavelength coverage.

ID	C4668 (Å)	Hβ (Å)	Fe5015 (Å)	Mg_1 (mag)	Mg_2 (mag)	Mgb (Å)	Fe5270 (Å)	Fe5335 (Å)	Fe5406 (Å)	Fe5709 (Å)	Fe5782 (Å)
g1566	(1.474)	1.994	2.692	(0.039)	(0.110)	1.895	1.668	(1.606)	0.832	0.467	0.242
	(0.180)	0.065	0.139	(0.001)	(0.002)	0.064	0.070	(0.080)	0.059	0.044	0.042
g296	0.339	(2.679)	1.676	(−0.039)	(0.028)	(1.027)	1.194	0.819	(0.778)	...	...
	0.382	(0.132)	0.283	(0.003)	(0.003)	(0.130)	0.142	0.163	(0.119)	...	...
g1940	1.193	2.153	2.816	(0.008)	(0.093)	2.045	1.745	1.425	(1.250)	(0.772)	0.178
	0.362	0.131	0.279	(0.003)	(0.003)	0.128	0.142	0.161	(0.117)	(0.087)	0.084
g1550	(3.430)	(1.100)	3.697	(0.085)	(0.198)	2.810	2.206	1.687	1.354	0.727	0.391
	(0.369)	(0.139)	0.287	(0.003)	(0.003)	0.133	0.143	0.163	0.118	0.089	0.085
g2122	2.411	1.670	3.940	(0.065)	(0.200)	2.953	2.387	(2.850)	1.546	0.590	(0.346)
	0.394	0.144	0.304	(0.003)	(0.004)	0.139	0.150	(0.165)	0.123	0.093	(0.089)
g1078	(3.035)	2.147	(4.188)	(0.025)	(0.112)	2.118	1.495	1.113	1.115	0.685	0.314
	(0.366)	0.134	(0.280)	(0.003)	(0.003)	0.130	0.144	0.165	0.119	0.087	0.084
g1420	1.273	(0.938)	(−0.436)	(0.038)	(0.115)	1.418	1.153	1.115	0.694	0.250	0.302
	0.380	(0.143)	(0.296)	(0.003)	(0.003)	0.136	0.147	0.166	0.121	0.093	0.088
g1540	(−1.675)	2.934	(−0.446)	(0.016)	(0.056)	1.441	0.717	0.898	(0.973)	(−0.433)	−0.156
	(0.414)	0.139	(0.325)	(0.003)	(0.004)	0.144	0.163	0.184	(0.133)	(0.101)	0.095
g1617	1.517	(1.131)	2.076	(−0.032)	(0.076)	2.534	1.268	0.814	0.354	0.288	0.163
	0.448	(0.169)	0.352	(0.003)	(0.004)	0.155	0.176	0.203	0.148	0.112	0.106
g1588	(−0.540)	2.255	(−0.892)	(0.081)	(0.167)	2.413	(3.422)	1.600	(−0.020)	0.700	(0.002)
	(0.546)	0.187	(0.418)	(0.004)	(0.005)	0.185	(0.195)	0.226	(0.175)	0.121	(0.118)
g114	(2.781)	2.327	2.621	(0.001)	(0.051)	1.230	1.687	1.310	0.706	...	...
	(0.558)	0.197	0.426	(0.004)	(0.005)	0.196	0.212	0.245	0.180	...	...
g1426	0.957	2.962	(−0.001)	(−0.067)	(−0.005)	2.373	(−1.293)	−0.045	0.920	(−0.364)	0.161
	0.570	0.196	(0.433)	(0.004)	(0.005)	0.188	(0.240)	0.267	0.188	(0.143)	0.131
g1610	0.796	2.451	3.175	(0.024)	(0.075)	(0.797)	0.906	0.900	0.419	...	...
	0.576	0.207	0.441	(0.004)	(0.005)	(0.208)	0.222	0.252	0.189	...	...
g1571	1.771	0.976	(0.318)	(0.085)	(0.157)	2.159	2.677	2.220	(0.742)	(−0.124)	0.705
	0.578	0.214	(0.464)	(0.004)	(0.005)	0.207	0.221	0.249	(0.192)	(0.138)	0.126
g1519	0.895	(0.468)	(6.229)	(−0.003)	(0.189)	(4.168)	(3.613)	1.874	(−0.074)	(1.240)	0.362
	0.549	(0.213)	(0.406)	(0.004)	(0.005)	(0.180)	(0.190)	0.226	(0.173)	(0.129)	0.126
g1934	0.258	3.209	(−2.122)	(−0.023)	(−0.052)	(−3.180)	1.031	0.496	(0.961)	0.157	−0.198
	0.662	0.231	(0.533)	(0.005)	(0.006)	(0.260)	0.264	0.301	(0.216)	0.168	0.167
g1580	2.831	(3.334)	(7.071)	(0.042)	(0.166)	(3.601)	2.713	(0.901)	(0.421)	0.856	(−0.083)
	0.696	(0.246)	(0.518)	(0.005)	(0.006)	(0.236)	0.260	(0.306)	(0.225)	0.163	(0.161)
g219	(−2.680)	2.595	0.108	(−0.034)	(0.043)	1.345	0.930	−0.152	0.715	...	...
	(0.809)	0.274	0.614	(0.006)	(0.007)	0.271	0.299	0.346	0.246	...	...
g1893	7.066	(3.030)	7.438	(0.111)	(0.250)	5.102	(4.318)	2.351	2.286	1.414	(0.316)
	0.818	(0.305)	0.615	(0.006)	(0.007)	0.273	(0.293)	0.345	0.254	0.191	(0.182)
g1630	(1.358)	2.091	(0.673)	(0.145)	(0.238)	2.505	2.254	2.013	(−0.329)	1.568	1.053
	(0.979)	0.354	(0.827)	(0.007)	(0.009)	0.351	0.366	0.417	(0.322)	0.219	0.212
g1595	(12.186)	2.914	0.448	(0.043)	(0.066)	(3.838)	−0.352	(−2.982)	−0.690	(1.311)	−0.223
	(1.024)	0.396	0.897	(0.009)	(0.010)	(0.366)	0.451	(0.543)	0.386	(0.268)	0.268
g230	(9.738)	(0.763)	0.969	(−0.113)	(0.067)	0.724	(4.403)	1.941	(−1.199)	...	...
	(1.046)	(0.442)	0.856	(0.008)	(0.010)	0.405	(0.395)	0.466	(0.388)	...	...

measured. Simultaneously a set of χ^2 minimization fits are found with each of the indices omitted. From this set, we select the fit with the lowest total χ^2, remove the necessary index and repeat until a stable fit is achieved with no highly aberrant ($>3\sigma$) indices remaining. All GCs had some indices that were significant outliers to the fit and therefore were removed during this process. For g1426 none of the indices potentially affected by the PN style emission lines are included in the final fit.

The molecular band indices Mg_1 and Mg_2 are systematically offset as a result of poor flux calibration and were excluded for all GCs (see Proctor et al. 2005). Similar to other GC studies (e.g. Beasley et al. 2004a), we find the CN indices to be

Table 4. Derived globular cluster properties. Age, [Fe/H], [E/Fe] and [*Z*/H] are derived from the χ^2 minimization process, with errors derived by a Monte Carlo-style method. $[Fe/H]_{BH}$ is derived according to the method of Brodie & Huchra (1990) from a reduced sample of indices.

ID	Age (Gyr)	[Fe/H] (dex)	[E/Fe] (dex)	[Z/H] (dex)	$[Fe/H]_{BH}$ (dex)
g1566	12.6 ± 1.1	-1.17 ± 0.05	0.15 ± 0.05	-1.03 ± 0.03	-1.15 ± 0.06
g296	11.2 ± 1.5	-1.82 ± 0.11	0.71 ± 0.10	-1.15 ± 0.06	-1.84 ± 0.26
g1940	11.9 ± 2.1	-1.26 ± 0.11	0.30 ± 0.10	-0.98 ± 0.06	-1.31 ± 0.12
g1550	15.0 ± 4.8	-0.69 ± 0.11	0.15 ± 0.07	-0.55 ± 0.11	-0.52 ± 0.18
g2122	15.0 ± 2.0	-0.47 ± 0.07	0.15 ± 0.06	-0.33 ± 0.04	-0.45 ± 0.10
g1078	10.0 ± 1.7	-1.05 ± 0.09	0.24 ± 0.09	-0.83 ± 0.06	-1.17 ± 0.06
g1420	10.0 ± 1.4	-1.40 ± 0.11	0.21 ± 0.09	-1.20 ± 0.06	-1.23 ± 0.10
g1540	9.4 ± 1.7	-2.09 ± 0.18	0.68 ± 0.17	-1.45 ± 0.09	-1.64 ± 0.04
g1617	11.2 ± 1.9	-1.52 ± 0.12	0.68 ± 0.10	-0.88 ± 0.08	-1.59 ± 0.28
g1588	8.4 ± 2.9	-0.57 ± 0.14	0.15 ± 0.09	-0.43 ± 0.13	-0.33 ± 0.16
g114	15.0 ± 6.5	-1.14 ± 0.16	-0.06 ± 0.15	-1.20 ± 0.14	-1.60 ± 0.17
g1426	7.5 ± 2.5	-1.58 ± 0.13	0.80 ± 0.07	-0.83 ± 0.11	-2.37 ± 0.44
g1610	10.6 ± 2.1	-1.62 ± 0.13	0.71 ± 0.12	-0.95 ± 0.09	-1.98 ± 0.40
g1571	15.0 ± 3.6	-0.10 ± 0.08	-0.27 ± 0.05	-0.35 ± 0.08	-0.29 ± 0.21
g1519	12.6 ± 2.9	-0.72 ± 0.13	-0.03 ± 0.10	-0.75 ± 0.09	-0.82 ± 0.37
g1934	10.0 ± 2.3	-2.31 ± 0.31	0.65 ± 0.29	-1.70 ± 0.15	-2.27 ± 0.21
g1580	9.4 ± 2.5	-0.24 ± 0.13	0.09 ± 0.09	-0.15 ± 0.09	-0.73 ± 0.12
g219	12.6 ± 1.8	-2.72 ± 0.37	0.50 ± 0.35	-2.25 ± 0.13	-2.15 ± 0.25
g1893	11.2 ± 5.9	0.12 ± 0.16	0.24 ± 0.09	0.35 ± 0.13	0.44 ± 0.05
g1630	11.2 ± 5.4	0.10 ± 0.19	-0.24 ± 0.08	-0.13 ± 0.19	0.20 ± 0.35
g1595	8.9 ± 3.2	-3.00 ± 0.49	0.80 ± 0.41	-2.25 ± 0.31	-2.08 ± 0.42
g230	15.0 ± 5.9	-1.52 ± 0.30	-0.30 ± 0.34	-1.80 ± 0.23	-2.34 ± 0.94

enhanced relative to the models and therefore they were also removed.

An index–index plot of $H\gamma_A$ versus Fe4383 is shown in Fig. 2. This pair of indices was chosen as the combination of an age- and a metallicity-sensitive index that had the largest number of reliable points. This shows that the majority of GCs lie near the 15 Gyr age line. Horizontal branch morphology is the apparent source of the offset to the left of the TMK04 15 Gyr age line seen in the majority of the low-metallicity GCs [see Pierce et al. (2005) for a brief discussion of the effect of horizontal branch morphology on GC χ^2 fitting]. The TMK04 models in this regime possess a predominantly blue horizontal branch, whereas the red horizontal branch models from Thomas, Maraston & Bender (2003) pass directly through these points. There are a couple of clear outliers for which one or both index values have been excluded from the fitting process. However, to derive values, we use the results from the χ^2 fitting process.

From our quantitative χ^2 minimization fits, we find all of the GCs to be consistent with an old age ($\gtrsim$10 Gyr) with a spread of metallicities from [Fe/H] < -2 to solar (Fig. 3). This is consistent with Fig. 2, and indeed the fitting procedure has identified clear outliers. The GC g1426, with the youngest fitted age of 7.5 Gyr, is the GC with unexplained emission lines in its spectrum. It also has α-element abundance ratio parameter [E/Fe] $= +0.8$, which is at the maximum of the models. While none of the clearly affected indices were included in the fit, we suspect that the fit was still somewhat influenced by the emission source.

A test of SSP-derived metallicities is to compare them with those derived using the (Brodie & Huchra 1990, hereafter BH) method. We were unable to use the full sample of metal-sensitive indices owing to the poor sensitivity at shorter wavelengths. We therefore measured the *G* band, Fe52, MgH and Mg_2 BH indices using the method outlined in their paper. We define a Brodie–Huchra metallicity as the average of the empirically calibrated metallicity from these four indices, where the error quoted is the standard deviation.

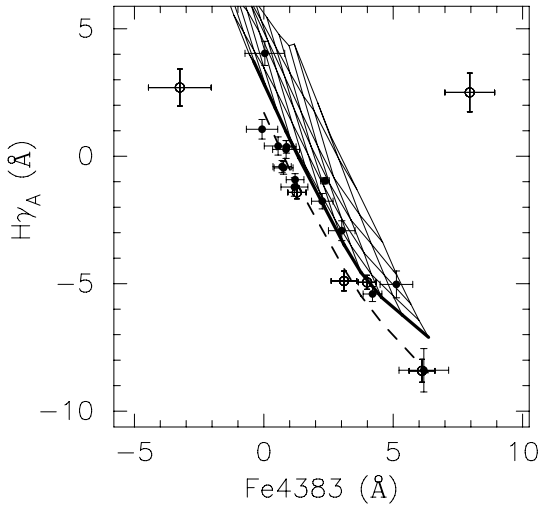

Figure 2. The indices $H\gamma_A$ versus Fe4383 are plotted against age–metallicity grids from TMK04. We show the grid for [E/Fe] $= +0.3$, with metallicity in 0.25 dex steps from from -2.25 (left) to $+0.5$ (right) and ages of 1, 2, 3, 5, 8, 12 and 15 Gyr (top to bottom). The bold line is 15 Gyr and the dashed line is the red horizontal branch 15 Gyr isochrone from Thomas et al. (2003). Filled circles are shown for GCs where both indices are included in the fits; if either index is excluded, then an open circle is plotted. A large number of the GCs fall near the maximum age line for the Thomas et al. (2003) red horizontal branch SSPs.

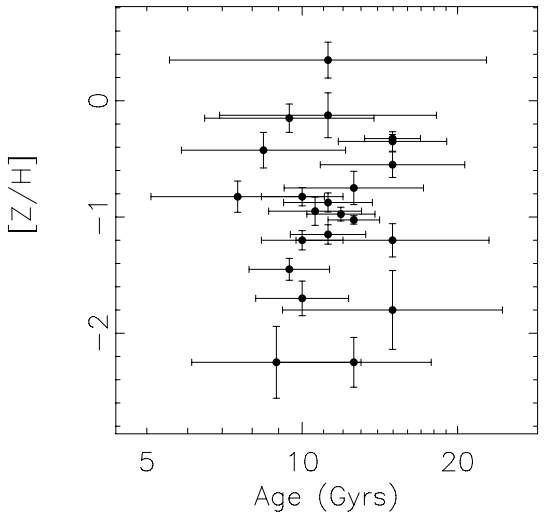

Figure 3. GC age–metallicity relation. The plot shows that the observed GCs are consistent with an old age and a wide range of metallicities.

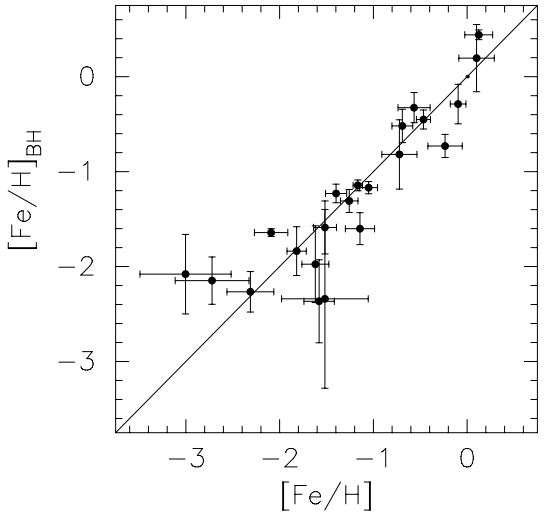

Figure 4. A comparison of Brodie–Huchra metallicity versus our derived metallicity. The four points with poor agreement at low metallicity (below $[Fe/H]_{BH} = -2$) are all at the limits of the SSP models. A gap in the metallicity distribution can be seen at $[Fe/H] \sim -1$, which resembles that of the Milky Way GC system.

This metallicity is referred to as $[Fe/H]_{BH}$ in Table 4. Fig. 4 shows that the BH metallicities closely match those derived by χ^2 fitting to SSPs. A gap in both metallicity measures occurs at $[Fe/H] \sim -1$. This is similar to that observed in the Milky Way GC system (Harris 1996), which is also composed of an old GC population. The outliers at low metallicity are at the limits of the SSP models for either [Fe/H] or [E/Fe].

We compare the observed $g - i$ colours for the GCs with the predicted $g - i$ colours from the Bruzual & Charlot (2003) SSPs, with the ages and metallicities from the TMK04 SSPs, in Fig. 5 (thus there could be some systematic offsets due to model differences). The use of the Bruzual & Charlot (2003) colour models is necessary because the TMK04 SSPs do not include *g* and *i* magnitudes. There are several outliers in the colour–colour plot; these include the low-metallicity GCs mentioned previously as well as a few others that are at the SSP model maximum age. A Spearman rank test gives the probability of correlation as 99.2 per cent. Overall, the figure gives us confidence in the SSP-derived parameters.

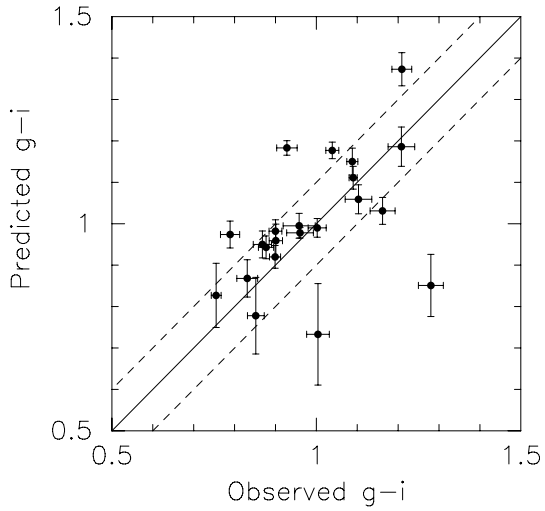

Figure 5. The predicted colour from stellar population fits versus observed $g - i$ colour. The outliers are GCs that are generally at the limits of the SSP models. The errors for both observed and predicted colours are lower limits and may be significantly underestimated. The dashed lines show the rms scatter of ±0.1 mag around the one-to-one full line. A Spearman rank test gives a probability of correlation of 99.2 per cent.

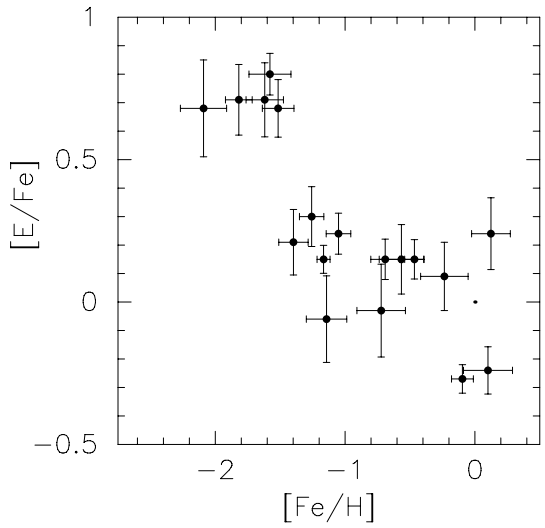

Figure 6. A plot of α-element abundance ratio versus metallicity. The four GCs with poorly determined metallicities and α-element abundance ratios (i.e. [E/Fe] errors > 0.3) are not shown. The plot indicates a correlation in the sense of increased enhancement with decreasing metallicity.

TMK04 estimate α-element abundance ratios using the parameter [E/Fe]. A definition of [E/Fe] for the SSP models used can be found in TMK04. Briefly, it includes α-elements, such as O, Ne, Mg, Si, S, Ar, Ca and Ti, plus two non-α-elements, N and Na. The [E/Fe] versus [Fe/H] plot presented in Fig. 6 shows decreasing α-element abundance ratio with increasing metallicity, including two solar-metallicity GCs with subsolar α-element abundance ratios. The source of this trend is confirmed by the index–index plots of Fig. 7, in which high-metallicity GCs generally have α-element sensitive indices that are consistent with [E/Fe] $<+$ 0.3.

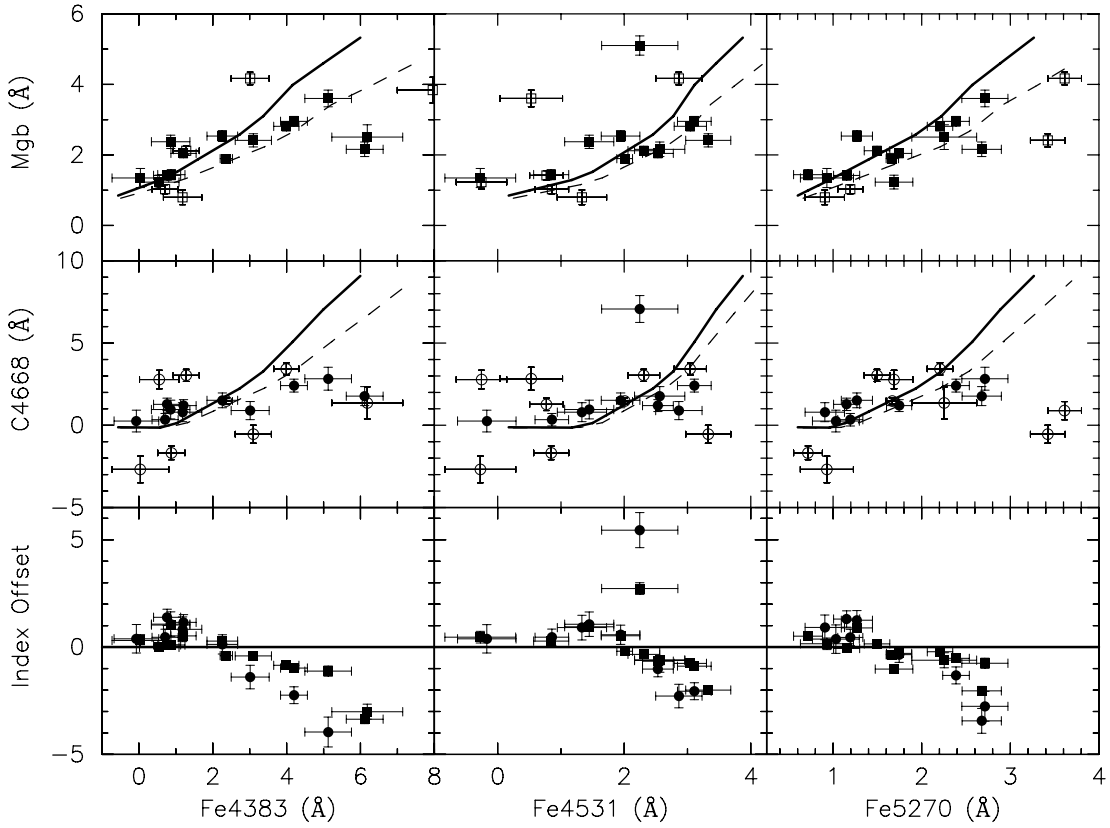

Figure 7. The upper row shows the α-element sensitive Mgb index versus three different iron indices (Fe4383, Fe4531 and Fe5270). The middle row shows C4668 versus the same iron indices. All six have TMK04 12 Gyr isochrones plotted with [E/Fe] = +0.3 (full line) and [E/Fe] = +0.0 (dashed line). Filled symbols show where both indices are included in the fit; if either of the indices is not included in the final fit, then open symbols are shown. For several plots, one or two highly aberrant indices fall outside the range plotted. All six plots show that the α-element sensitive indices are above the [E/Fe] = +0.3 dex model at low iron-sensitive index values and are below for high iron values. The bottom row of plots shows the index offset relative to the [E/Fe] = +0.3 dex model line, for included indices. Squares are Mgb and circles are C4668. A strong trend of decreasing α-element abundance ratio with increasing iron abundance is seen for both α-element sensitive indices relative to the [E/Fe] = +0.3 model expectation.

The lower-metallicity GCs have α-element sensitive indices that are predominantly stronger than [E/Fe] = +0.3.

4 GLOBULAR CLUSTER KINEMATICS

In this section we use our measured velocities for 22 GCs (see Table 1) to estimate the radial velocity dispersion and mass-to-light ratio for the halo of NGC 3379. Our sample is supplemented by measurements of 14 GC velocities from Puzia et al. (2004), who used the FORS instrument on the VLT.

The spatial distribution of the combined 36 GCs, in relation to NGC 3379 and 3384, is shown in Fig. 8. From this figure, it can be seen that four of the GCs (from our GMOS sample) lie roughly half-way between NGC 3379 and 3384. As NGC 3379 is more luminous than NGC 3384 (M_V of −21.06 versus −20.64), we might expect NGC 3379 to have the more populous GC system, and indeed this seems to be the case (Whitlock et al. 2003). The average velocity of the four GCs is $924 \pm 46\,\mathrm{km\,s^{-1}}$. The systemic velocity of NGC 3379 is $911\,\mathrm{km\,s^{-1}}$. For NGC 3384, the systemic velocity is $704\,\mathrm{km\,s^{-1}}$; however, NGC 3384 has a substantial rotation (it is an S0 galaxy). The rotation amplitude is about $200\,\mathrm{km\,s^{-1}}$ (Fisher 1997) and the side closest to NGC 3379 is redshifted. Any rotation in the NGC 3379 GC system is below 2σ significance at all radii and the sample is consistent with no rotation. In the unlikely situation of the NGC 3384 rotating disc extending to several effective radii, and that the four GCs in question are part of the NGC 3384 disc population, the expected mean velocity of NGC 3384 members would be essentially the same as that for NGC 3379. Therefore, the membership of these four GCs is not entirely clear. We run the dynamical models below, both including and excluding these four GCs, but our conclusions are not greatly affected either way.

Ideally, the best estimate of the mass-to-light (M/L) variation would come from models without assumptions about the distribution function. The state of the art is to use orbit-based models (e.g. Gebhardt et al. 2003; Thomas et al. 2005). However, with only 36 clusters it is not practicable to run these flexible models. For an estimate of the M/L variation at large radii, we instead employ isotropic models. While there are theoretical concerns for assuming isotropy at large radii, these models provide a comparative base to other studies.

For an isotropic model, we only require the second moment of the projected velocity distribution. The data on the inner parts of the galaxy come from Gebhardt et al. (2000) and Statler & Smecker-Hane (1999). For the velocity dispersion profile from the GC system, we use a 'lowess' estimator (explained in detail in Gebhardt et al. 1995). The lowess technique effectively runs a radial window function through the data to estimate the velocity squared. It takes the velocity uncertainties into account directly. We have checked this estimator against a variety of dispersion estimates, including maximum likelihood, and find no significant differences.

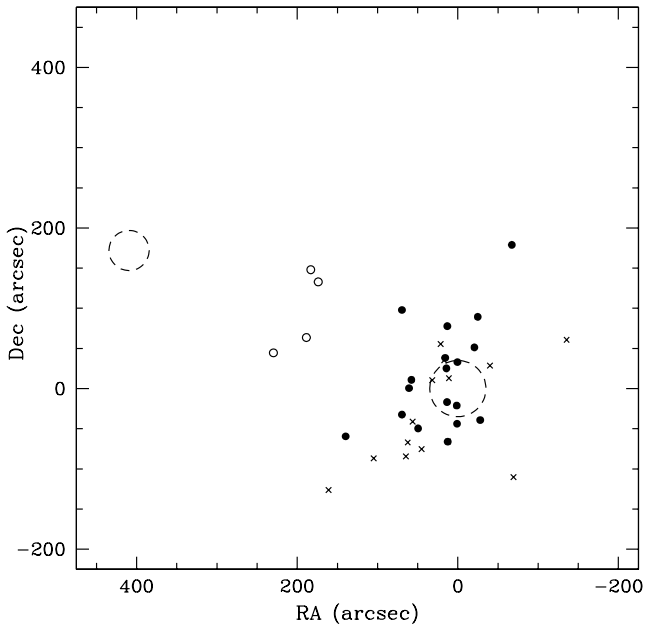

Figure 8. Spatial positions of GCs. The filled circles are GMOS data presented here; crosses are VLT data of Puzia et al. (2004). The two large circles show the effective radius of the galaxies NGC 3379 (lower right) and NGC 3384 (upper left) (de Vaucoulurs et al. 1991; Cappaccioli et al. 1990). The effective radius for NGC 3379 is 55 arcsec (4.4 kpc). The four GCs approximately midway between NGC 3379 and 3384 most likely belong to NGC 3379; however, they cannot be decisively assigned to either galaxy and are therefore shown as open circles.

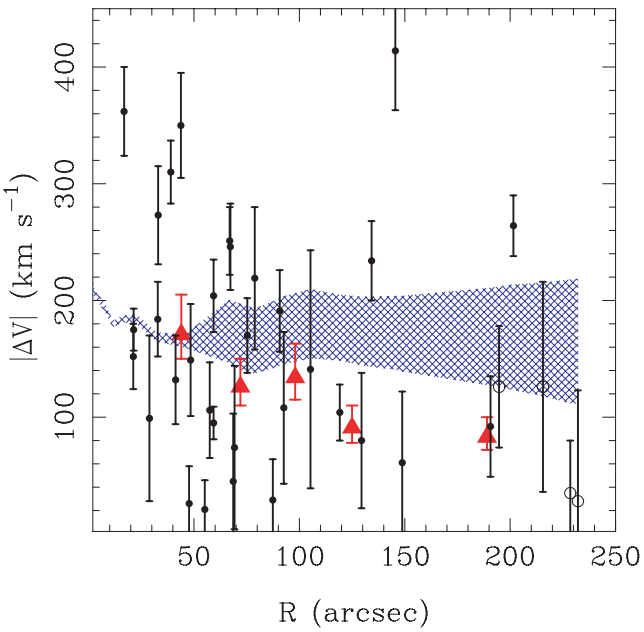

Figure 9. Absolute velocity differences between GCs and the systemic velocity of NGC 3379 (911 km s^{-1}) with projected galactocentric radius. The filled circles are GMOS and VLT data presented here; open circles indicate the four GCs that are possibly associated with NGC 3384; the triangles (in red in the online version of this article) are the binned PN data of Romanowsky et al. (2003). The (blue) cross-hatched region shows the 1σ confidence interval for the velocity dispersion from the lowess estimator, including all GCs.

Fig. 9 shows the line-of-sight velocity with projected radius for the individual GCs. This allows a comparison of our unsmoothed data with the lowess estimator velocity dispersion and the binned Romanowsky et al. (2003) PN data. The individual data point at $R \sim 150$ arcsec with $|\Delta V| \sim 400\,\mathrm{km\,s^{-1}}$ has a relatively large velocity difference, which increases the velocity dispersion at large radii. If we remove this one point, then the dispersion is reduced from $166\,\mathrm{km\,s^{-1}}$ to $125\,\mathrm{km\,s^{-1}}$ at the largest radii (which are the most uncertain). When compared to the PN dispersion, this results in a 3.5σ difference as opposed to a 4σ difference when the full sample is used. The technique we are using for the dispersion has some robustness to outliers built in already, which is why the change in statistical significance is not particularly strong.

The top panel in Fig. 10 plots the dispersion profile combining both the stellar and globular cluster data. In the overlap region the agreement in the dispersion estimates is very good. The 68 per cent confidence bands come from Monte Carlo simulations as detailed in Gebhardt et al. (1995).

We use non-parametric, isotropic models as outlined in Gebhardt & Fischer (1995). Given the surface brightness profile and velocity dispersion profile, the spherical Jeans equation can uniquely determine the mass density profile (and hence the M/L profile) assuming isotropy. Through the Abel deprojection, the surface brightness profile uniquely determines the luminosity density. Similarly, the surface brightness times the projected velocity dispersion determines the luminosity density times the internal (3D) velocity dispersion. From the internal velocity dispersion, we can derive the mass profile and hence the M/L profile. We employ a degree of smoothing since the Abel deprojection involves a derivative (Gebhardt et al. 1996).

The surface brightness profile for the kinematic tracer is important to characterize well for the dynamical analysis. We use the globular cluster number density profile from Rhode & Zepf (2004). Their data extend from 1.2 arcmin to approximately 20 arcmin. The surface brightness profile for the stellar light comes from Gebhardt et al. (2000), which extends to 2.8 arcmin. Thus, there is significant overlap for comparison. In the overlap region, the stellar light is slightly steeper than the GC profile, and after 2.5 arcmin the GC profile flattens significantly. For the dynamical analysis, one should use the GC profile only; however, in order to deproject properly, one requires the central profile, which does not exist for the GCs. Thus, we have to rely somewhat on the stellar profile for the extrapolation inwards. For the dynamical analysis, we use the GC profile from Rhode & Zepf (2004) in to 1.2 arcmin, and then use the stellar profile interior to that. We have also tried a variety of profiles: using only the cluster profile with various central extrapolations; using only the stellar light profile; and using various extrapolations to larger radii. We find that there is essentially no effect from the large radii extrapolation. For the small radii extrapolation, the effect on the projected dispersion is dramatic at small radius but relatively insignificant at the radii where we have GC velocities. Thus, all of our tests suggest there is little effect on our overall results from the surface brightness profile.

The velocity dispersion and M/L ratio are plotted with galactocentric radius in Fig. 10. GC data, both including and excluding the four GCs potentially associated with NGC 3384, are shown. The solid line in the upper panel in Fig. 10 is the expected isotropic velocity dispersion profile for a constant M/L ratio, which is consistent with the Romanowsky et al. (2003) PN data. In the bottom panel we plot the projected M/L profile, calculated by the lowess method and using the surface brightness profile characterization described above. Both cases (including and excluding the four GCs) show a

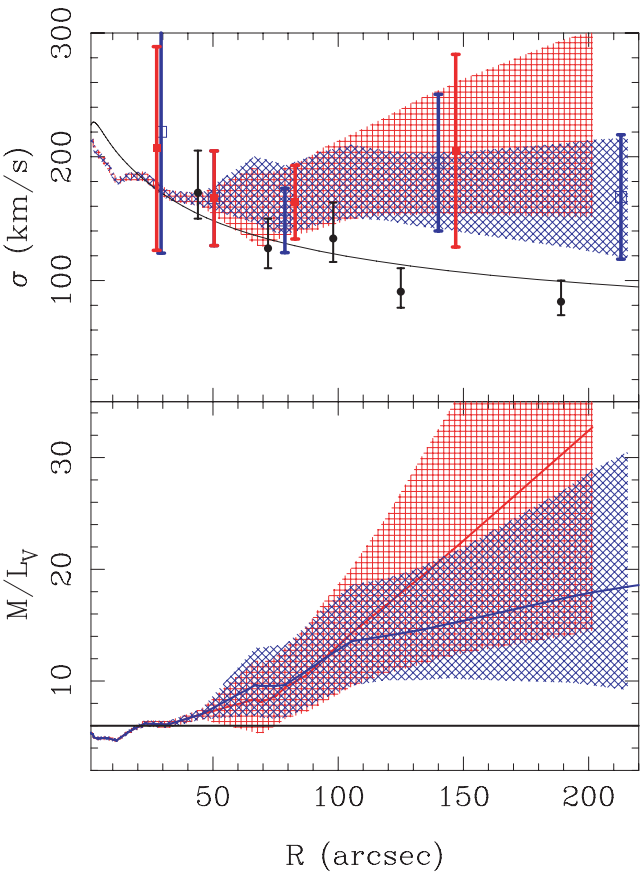

Figure 10. Plots of radial velocity dispersion and M/L ratio using GC and stellar data (from Gebhardt et al. 2000 and Statler & Smecker-Hane 1999). The upper panel shows the velocity dispersion of the GCs. The (blue) open squares and diagonal cross-hatching include the four GCs that may be associated with NGC 3384; and the (red) filled squares and vertical/horizontal hatching when they are excluded. The squares show the binned data and the hatched areas show the range of values using the lowess estimator (with 1σ errors). The PN data points from Romanowsky et al. (2003) (full circles) and the expected isotropic profile with constant M/L (full line) are also shown. In the lower panel, the (blue) lower line (with 1σ diagonal cross-hatching) shows that when the four ambiguous GCs are included the M/L ratio rises slowly. The (red) upper line (with 1σ vertical/horizontal hatching) shows that the M/L ratio rises strongly in the outer regions when the four ambiguous GCs are excluded. The horizontal line in the bottom panel is $M/L = 6$. See text for details.

rise in the M/L at large radii. This rise in M/L is stronger when the four GCs are excluded.

Finally, we remind the reader that the above results are based on only 36 GCs as kinematic tracers; clearly such an analysis should be repeated when larger samples become available.

5 DISCUSSION

The reliability of the GC parameters derived from Lick indices and our χ^2 fitting method are affected by several factors, most importantly the stability of the fit when individual indices are excluded. For some GCs it is not possible to find a stable fit that includes a large number of indices (>10). This is often the case for the low-S/N GCs. The large index errors of low-S/N GCs mean that, within 3σ, the indices can be consistent with a wide range of ages and metallicities. In this situation the fit can be driven by a single index that is outside the range spanned by the models, leading to a fit at the extreme of the SSP models. When this occurs the Monte Carlo-determined errors are large, reflecting the lower accuracy of these parameters.

To examine the effects of these factors, we tested the reliability of the χ^2 fitted metallicities by comparing them to Brodie–Huchra metallicities. Fig. 4 shows the good agreement between the two metallicity measures, with some divergence below [Fe/H] $= -2$ dex. We then used $g - i$ colour as a test of the derived age and metallicity. Model predictions for $g - i$ from Bruzual & Charlot (2003), for our χ^2 fitted ages and metallicities (derived using TMK04 SSPs), are plotted against the observed $g - i$ colours in Fig. 5. We see reasonable agreement between the predicted and observed colours, with the outliers being those low-S/N GCs that are at the limits of the models.

Having established the reliability of our χ^2 minimization fits for age and metallicity, we find that all of the GCs are consistent with an old age ($\gtrsim$10 Gyr) within errors, and a spread of metallicities is seen, from [Fe/H] < -2 to solar (see Fig. 3). We see no discernible age structure.

We next consider the α-element abundance ratio parameter [E/Fe]. Because of the necessary exclusion of the Mg and CN indices (see Section 3), the only strongly α-element sensitive indices included in the fits are Mgb and C4668. However, all the plots of Mgb and C4668 against Fe-sensitive indices (Fig. 7) display the same overall trend, one of decreasing α-element abundance ratio with increasing metallicity. This is highlighted by plotting the residuals of the model [E/Fe] $= +0.3$ line to these index pairs. This is also seen for [E/Fe] derived from the χ^2 fitting process (Fig. 6). A similar trend is apparent for GCs in NGC 1052 (see fig. 9 of Pierce et al. 2005) and is also noted in Puzia et al. (2005). This contrasts with the findings of Carney (1996) for Galactic GCs in which [α/Fe] is largely constant for GCs of all metallicities. However, the Puzia et al. (2005), NGC 3379 and 1052 results are derived from TMK04 models. These models were constructed using the results of Tripicco & Bell (1995), which included the effects of α-element variation on stars of solar metallicity. The application of the Tripicco & Bell models to GCs of [Fe/H] ~ -2 may therefore play a part in generating the observed trend of high α-element abundance ratios for GCs at low metallicity. At such low metallicity we can see from Fig. 7 that the indices cannot offer much leverage to differentiate the [E/Fe] values.

However, we note that the α-element abundance ratio trend extends up to the solar metallicity at which the Tripicco & Bell (1995) models were calculated. Of particular interest are the two GCs with solar metallicity, [E/Fe] ~ -0.25 and ages greater than 10 Gyr. While there is no obvious link, it is interesting to note that X-ray observations of hot gas in the centre of the NGC 5044 galaxy group reveal a similar abundance pattern, of a subsolar α-element abundance ratio at solar metallicity (Buote et al. 2003). A significant number of Type Ia, rather than Type II, supernovae are therefore necessary to produce enough iron to explain this abundance pattern. Such a process must have occurred rapidly due to the old ages of the GCs.

From the measured recession velocities of our sample of 22 GCs, and 14 GCs from Puzia et al. (2004), we find evidence for a significant dark matter halo. This result does not depend on the inclusion of four GCs that may belong to NGC 3384. The PN data of Romanowsky et al. (2003) showed a decrease in velocity dispersion at large radii, suggesting a minimal DM halo. However, Dekel et al. (2005) recently showed that stellar orbits in the outer regions of merger-remnant elliptical galaxies are elongated and that declining

PN velocity dispersions do not necessarily imply a dearth of dark matter. This demonstrates that the orbital properties of the kinematic tracers need to be well understood. For PN radial orbits need to be included, while for GCs isotropic models should be sufficient (see Cote et al. 2003), but caution is still required. Ignoring the differences between dynamical models, we still find that the results from the two studies contradict each other.

A two-sided χ^2 test over all radii using all GCs gives a 2σ difference between the mass profile derived from our GCs compared to the PN-derived mass model of Romanowsky et al. (2003). This would indicate a borderline statistical difference between our mass model and the 'no dark matter' model of Romanowsky et al.

To test the significance of the differences between the PN and GC data, we have carried out a Monte Carlo simulation. At the radius of a given PN binned data point, we sample from a Gaussian distribution using a mean given by the GC lowess dispersion estimate and the standard deviation from the 68 per cent confidence band at that point. We draw another Gaussian from the PN value and its uncertainty. We then ask whether the new PN dispersion is smaller than the new GC dispersion at that point. For a single measurement, this is only a χ^2 test; however, generalizing for a range of radii, we determine whether each of the PN dispersions are smaller than each of the GC dispersions. This test is rather strict in the sense that, if any realization shows one PN value above the GC value at that radius, then the difference is not considered. At small radii, the PN and GC dispersions are consistent, whereas at large radii, the PN dispersions are lower.

We find that the PN dispersions are smaller than the GC dispersions at >97 per cent confidence beyond an effective radius. Since the PN dispersions are consistent with mass following light, the GC dispersions suggest a need for a dark halo. Either the orbital properties of the two tracers are different (Dekel et al. 2005), or one or both are hampered by low number statistics.

Two alternative observations suggest the presence of a dark matter halo around NGC 3379. *Chandra* archival data for NGC 3379 indicate that a hot gaseous halo is present (Fukazawa et al. 2006). The kinematics of the H I gas ring around the Leo triplet of NGC 3379, 3384 and 3389 suggests a mass-to-light ratio of 27, which is consistent with a DM halo (Schneider 1989).

One possible explanation for the difference between the PN data and the indication of a normal DM halo could be that NGC 3379 is a face-on S0 galaxy, as suggested by Capaccioli et al. (1991). If a significant fraction of the PN belong to a disc, this would suppress the line-of-sight velocity dispersion of the PN relative to that of the GCs which lie in a more spherical halo.

6 CONCLUSIONS

We have obtained Gemini/GMOS spectra for 22 GCs around the elliptical galaxy NGC 3379. We present ages, metallicities and α-element abundance ratios that were derived by applying the multi-index χ^2 minimization method of Proctor & Sansom (2002) to the SSP models of Thomas et al. (2004). Metallicity estimates, derived according to the method of Brodie & Huchra (1990), agree closely with those from our χ^2 minimization method. We also find good agreement between the observed colours and those predicted from our χ^2 minimization method ages and metallicities. All the GCs are found to be consistent with old ages, i.e. $\gtrsim$10 Gyr, with a wide range of metallicities. This is consistent with the resolved stellar population work of Gregg et al. (2004), who found the galaxy stars in the outer regions to be old. We find no evidence for a young GC subpopulation.

The α-element abundance ratios appear to decrease with increasing metallicity; however, interpretation of this trend is complex and requires further work.

Using the recession velocities of our 22 GCs and 14 GCs from Puzia et al. (2004), we measure the projected velocity dispersion of the GC system and find that it is consistent with being constant with radius in the outer regions. With this velocity dispersion profile, NGC 3379 appears to possess a dark halo, although we cannot rigorously determine the dark halo mass. This is in contrast to the earlier claims of Romanowsky et al. (2003) of a minimal DM halo, based on PN kinematics.

A two-sided χ^2 test over all radii using all GCs gives a 2σ difference between the mass profile derived from our GCs compared to the PN-derived mass model of Romanowsky et al. (2003). This would indicate a borderline statistical difference between our mass model and the 'no dark matter' model of Romanowsky et al. However, if we restrict our analysis to radii beyond one effective radius and test if the GC velocity dispersion is consistently higher, then we determine a $>3\sigma$ difference between the mass models, and hence favour the conclusion that NGC 3379 does indeed have dark matter at large radii in its halo.

ACKNOWLEDGMENTS

We thank the Gemini support staff for help preparing the slit mask. We thank S. Brough, A. Romanowsky and S. Samurovic for useful comments. DAF thanks the ARC for its financial support. SEZ acknowledges support for this work in part from the NSF grant AST-0406891 and from the Michigan State University Foundation. This research was supported in part by a Discovery Grant awarded to DAH by the Natural Sciences and Engineering Research Council of Canada (NSERC).

These data were based on observations obtained at the Gemini Observatory, which is operated by the Association of Universities for Research in Astronomy, Inc., under a cooperative agreement with the NSF on behalf of the Gemini partnership: the National Science Foundation (United States), the Particle Physics and Astronomy Research Council (United Kingdom), the National Research Council (Canada), CONICYT (Chile), the Australian Research Council (Australia), CNPq (Brazil), and CONICET–Agencia Nac. de Promocion Cientifica y Tecnologica (Argentina). The Gemini programme ID is GN-2003A-Q22. This research has made use of the NASA/IPAC Extragalactic Database (NED), which is operated by the Jet Propulsion Laboratory, Caltech, under contract with the National Aeronautics and Space Administration.

NOTES ADDED IN PROOF

We emphasize that the mass model we compare to, and find discrepancy with, is an isotropic constant *M/L* model, which is the simplest interpretation of the PN data implying no DM. This is not the same as the preferred mass model presented in Romanowsky et al. (2003), which was an orbit model including some DM. For detailed comparison to such a model, the dynamical characteristics and projection effects for both the GCs and PN would need to be taken into account, which is beyond the scope of this work.

Our attention was drawn to the paper by Samurovic & Danziger (2005). Their analysis of the X-ray halo of NGC 3379 leads to predictions of both *M/L* and velocity dispersion with radius that are consistent with those from our GC analysis. For example, see their figs 10 and 12, and their statement 'We note that beyond 120 arcsec

($\sim 2.2 R_e$) discrepancy between PNe estimates and X-ray estimate occurs'.

REFERENCES

Ashman K. M., Zepf S. E., 1992, ApJ, 384, 50
Beasley M. A., Baugh C. M., Forbes D. A., Sharples R. M., Frenk C. S., 2002, MNRAS, 333, 383
Beasley M. A., Brodie J. P., Strader J., Forbes D. A., Proctor, R. N., Barmby P., Huchra J. P., 2004a, AJ, 128, 1623
Beasley M. A., Forbes D. A., Brodie J. P., Kissler-Patig M., 2004b, MNRAS, 347, 1150
Bertin E., Arnouts S., 1996, A&AS, 117, 393
Bridges T. J., 1992, PhD thesis, Queen's Univ., Kingston, Ontario
Bridges T. J. et al., 2003, in Bridges T., Forbes D., eds, 25th IAU General Assembly, JD6, Extragalactic Globular Clusters and Their Host Galaxies. Astron. Soc. Pac., San Francisco, in press (astro-ph/0310324)
Brodie J. P., Huchra J. P., 1990, ApJ, 362, 503 (BH)
Brodie J. P., Strader J., Denicolo G., Beasley M. A., Cenarro A. J., Larsen S. S., Kuntschner H., Forbes D. A., 2005, AJ, 129, 2643
Bruzual A. G., Charlot S., 2003, MNRAS, 344, 1000
Buote D. A., Lewis A. D., Brighenti F., Mathews W. G., 2003, ApJ, 595, 151
Capaccioli M., Held E. V., Lorenz H., Vietri M., 1990, AJ, 99, 1813
Capaccioli M., Vietri M., Held E. V., Lorenz H., 1991, ApJ, 371, 535
Carney B. W., 1996, PASP, 108, 900
Cote P., Marzke R. O., West M. J., 1998, ApJ, 501, 554
Cote P. et al., 2001, ApJ, 559, 828
Cote P., McLaughlin D. E., Cohen J. G., Blakeslee J. P., 2003, ApJ, 591, 850
Cowie L. L., Songaila A., Hu E. M., Cohen J. G., 1996, AJ, 112, 839
Davies R. L., Burstein D., Dressler A., Faber S. M., Lynden-Bell D., Terlevich R. J., Wegner G., 1987, ApJS, 64, 581
Dekel A., Stoehr F., Mamon G. A., Cox T. J., Primach J. R., 2005, Nat, 437, 707
de Vaucouleurs G., de Vaucouleurs A., Corwin H. G., Buta R. J., Paturel G., Fouque P., 1991, Sky Telesc., 82, 821
Fisher D., 1997, AJ, 113, 950
Forbes D. A., Brodie J. P., Grillmair C. J., 1997, AJ, 113, 1652
Forbes D. A., Beasley M. A., Brodie J. P., Kissler-Patig M., 2001, ApJ, 563, 143
Forbes D. A. et al., 2004, MNRAS, 355, 608
Fukazawa Y., Betoya-Nonesa J. G., Pu J., Ohto A., Kawano N., 2006, ApJ, 636, to appear (astro-ph/0509521)
Gebhardt K., Fischer P., 1995, AJ, 109, 209
Gebhardt K., Kissler-Patig M., 1999, AJ, 118, 1526
Gebhardt K., Pryor C., Williams T. B., Hesser J. E., 1995, AJ, 110, 1699
Gebhardt K., Richstone D., Ajhar E. A., Kormendy J., Dressler A., Faber S. M., Grillmair C., Tremaine S., 1996, AJ, 112, 105
Gebhardt K. et al., 2000, AJ, 119, 1157
Gebhardt K. et al., 2003, ApJ, 583, 92
Goudfrooij P., Mack J., Kissler-Patig M., Meylan G., Minniti D., 2001, MNRAS, 322, 643
Gregg M. D., Ferguson H. C., Minniti D., Tanvir N., Catchpole R., 2004, AJ, 127, 1441
Harris W. E., 1996, AJ, 112, 1487
Harris W. E., 1999, Ap&SS, 267, 95
Hook I. et al., 2002, Proc. SPIE 4841, Power Telescopes and Instrumentation into the New Millennium. SPIE, Bellingham, WA
Kodama T. et al., 2005, PASJ, 57, 309
Kundu A., Whitemore B. C., 2001, AJ, 121, 2950
Kuntschner H., Ziegler B. L., Sharples R. M., Worthey G., Fricke K. J., 2002, A&A, 395, 761
Larsen S. S., Brodie J. P., 2002, AJ, 123, 1488
Larsen S. S., Brodie J. P., Huchra J. P., Forbes D. A., Grillmair C. J., 2001, AJ, 121, 2974
Macchetto F., Pastoriza M., Caon N., Sparks W. B., Giavalisco M., Bender R., Capaccioli M., 1996, A&A, 120, 463
Minniti D., Rejkuba M., 2002, ApJ, 575, L59
Peng E. W., Ford H. C., Freeman K. C., 2004, ApJ, 602, 705
Pierce M. J., Brodie J. P., Forbes D. A., Beasley M. A., Proctor R. N., Strader J., 2005, MNRAS, 358, 419
Proctor R. N., Sansom A. E., 2002, MNRAS, 333, 517
Proctor R. N., Forbes D. A., Beasley M. A., 2004, MNRAS, 355, 1327
Proctor R. N., Forbes D. A., Forestell A., Gebhardt K. 2005, MNRAS, 362, 857
Puzia T. H. et al., 2004, A&A, 415, 123
Puzia T. H., Kissler-Patig M., Thomas D., Maraston C., Saglia R. P., Bender R., Goudfrooij P., Hempel M., 2005, A&A, 439, 997
Rhode K. L., Zepf S. E., 2004, AJ, 127, 302
Richtler T. et al., 2004, AJ, 127, 2094
Romanowsky A. J., Douglas N. G., Arnaboldi M., Kuijken K., Merrifield M. R., Napolitano N. R., Capaccioli M., Freeman K. C., 2003, Sci, 301, 1696
Samurovic S., Danziger I. J., 2005, MNRAS, 363, 769
Schlegel D. J., Finkbeiner D. P., Davis M., 1998, ApJ, 500, 525
Schneider S. E., 1989, ApJ, 343, 94
Schweizer F., Seitzer P., 1992, AJ, 104, 1039
Statler T., Smecker-Hane T., 1999, AJ, 117, 839
Strader J., Brodie J. P., Schweizer F., Larsen S. S., Seitzer P., 2003, AJ, 125, 626
Strader J., Brodie J. P., Forbes D. A., 2004, AJ, 127, 295
Terlevich A. I., Forbes D. A., 2002, MNRAS, 330, 547
Thomas D., Maraston C., Bender R., 2003, MNRAS, 339, 897
Thomas D., Maraston C., Korn A., 2004, MNRAS, 351, 19 (TMK04)
Thomas J., Saglia R. P., Bender R., Thomas D., Gebhardt K., Magorrian J., Corsini E. M., Wegner G., 2005, MNRAS, 360, 1355
Trager S. C., Worthey G., Faber S. M., Burstein D., Gonzalez J. J., 1998, ApJS, 116, 1
Trager S. C., Faber S. M., Worthey G., Gonzalez J. J., 2000, AJ, 119, 1645
Tripicco M. J., Bell R. A., 1995, AJ, 110, 3035
van Dokkum P. G., Franx M., 1995, AJ, 110, 2027
Whitlock S., Forbes D. A., Beasley M. A., 2003, MNRAS, 345, 949
Worthey G., 1994, ApJS, 95, 107
Zepf S. E., Beasley M. A., Bridges T. J., Hanes D. A., Sharples R. M., Ashman K. M., Geisler D., 2000, AJ, 120, 2928

This paper has been typeset from a TEX/LATEX file prepared by the author.